NANO LETTERS
Letter
Cite This: Nano Lett. 2018, 18, 3352−3361
pubs.acs.org/NanoLett

Role of Carbon Interstitials in Transition Metal Substrates on Controllable Synthesis of High-Quality Large-Area Two-Dimensional Hexagonal Boron Nitride Layers

Hao Tian,[†] Alireza Khanaki,[†] Protik Das, Renjing Zheng, Zhenjun Cui, Yanwei He, Wenhao Shi, Zhongguang Xu, Roger Lake, and Jianlin Liu*

Department of Electrical and Computer Engineering, University of California, Riverside, California 92521, United States

Supporting Information

ABSTRACT: Reliable and controllable synthesis of two-dimensional (2D) hexagonal boron nitride (h-BN) layers is highly desirable for their applications as 2D dielectric and wide bandgap semiconductors. In this work, we demonstrate that the dissolution of carbon into cobalt (Co) and nickel (Ni) substrates can facilitate the growth of h-BN and attain large-area 2D homogeneity. The morphology of the h-BN film can be controlled from 2D layer-plus-3D islands to homogeneous 2D few-layers by tuning the carbon interstitial concentration in the Co substrate through a carburization process prior to the h-BN growth step. Comprehensive characterizations were performed to evaluate structural, electrical, optical, and dielectric properties of these samples. Single-crystal h-BN flakes with an edge length of ∼600 μm were demonstrated on carburized Ni. An average breakdown electric field of 9 MV/cm was achieved for an as-grown continuous 3-layer h-BN on carburized Co. Density functional theory calculations reveal that the interstitial carbon atoms can increase the adsorption energy of B and N atoms on the Co(111) surface and decrease the diffusion activation energy and, in turn, promote the nucleation and growth of 2D h-BN.

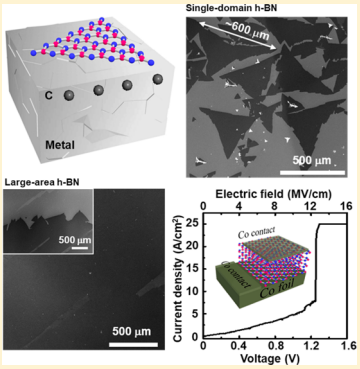

KEYWORDS: *Hexagonal boron nitride (h-BN), molecular beam epitaxy (MBE), interstitial carbon, large domain size, breakdown electric field*

Hexagonal boron nitride (h-BN), a two-dimensional (2D) isostructure of graphene, has gained significant attention for its remarkable properties,[1−3] as well as its potential applications as a 2D dielectric[4−7] and a wide bandgap semiconductor material.[3,8,9] To realize the technological potential of h-BN, the key is reliable and controllable synthesis of large-area h-BN. Toward this direction, tremendous effort has been made on chemical vapor deposition (CVD) of h-BN on various catalytic transition metal substrates, including Cu,[2,10−12] Co,[13] Ni,[14−16] Fe,[17−19] Ru,[20] and Pt.[21] Experiments have proven that transition metals can provide a favorable chemical environment for the synthesis of high-quality graphene and h-BN. In addition, rational engineering of catalytic effects of the transition metal substrates by alloying or incorporating additional species has been utilized in the growth of both h-BN and graphene to enhance the control over layer number, nucleation density, and domain size.[17,19,22] Recently, CVD growth of graphene and h-BN assisted by carbon in the form of α-C or hydrocarbon gas has been reported by predepositing PMMA[23] or simultaneously introducing methane,[24] respectively. Nevertheless, the growth of h-BN on transition metal substrates incorporated with carbon as interstitial atoms has not been studied. Transition metals with high carbon solubility are commonly thought to be detrimental for graphene growth, due to the precipitation of low-quality graphitic structure during substrate cooling, resulting in poor layer number controllability.[25] However, from a completely different perspective, the high carbon solubility of metals ensures the presence of a substantial amount of dissolved carbon atoms as interstitials. As a result, the tuning of carbon concentration in a wide range within the carbon solubility's limit can bring a new dimension of control for the growth of h-BN in addition to other regular growth parameters such as substrate temperature, growth pressure, surface roughness, and so on. Thus, to elucidate the effect of interstitial carbon on the growth of h-BN, it is essential to control the carbon concentration precisely at a trace level so that the carbon atoms do not end up precipitating onto the metal surface. From this standpoint, molecular beam epitaxy (MBE), an alternative to CVD, has the ability to precisely control solid, gas, and plasma sources and tune the growth parameters. Some general comparison of MBE and CVD for 2D material synthesis can be found elsewhere,[26−35] and MBE has been demonstrated to be a reliable method to grow 2D h-BN and h-BN/graphene heterostructures.[26−35]

In this work, we carefully prepared Co and Ni substrates with different carburization times using acetylene gas prior to the growth of h-BN in a plasma-assisted MBE system. The

Received: December 8, 2017
Revised: April 21, 2018
Published: May 4, 2018

DOI: 10.1021/acs.nanolett.7b05179
Nano Lett. 2018, 18, 3352−3361

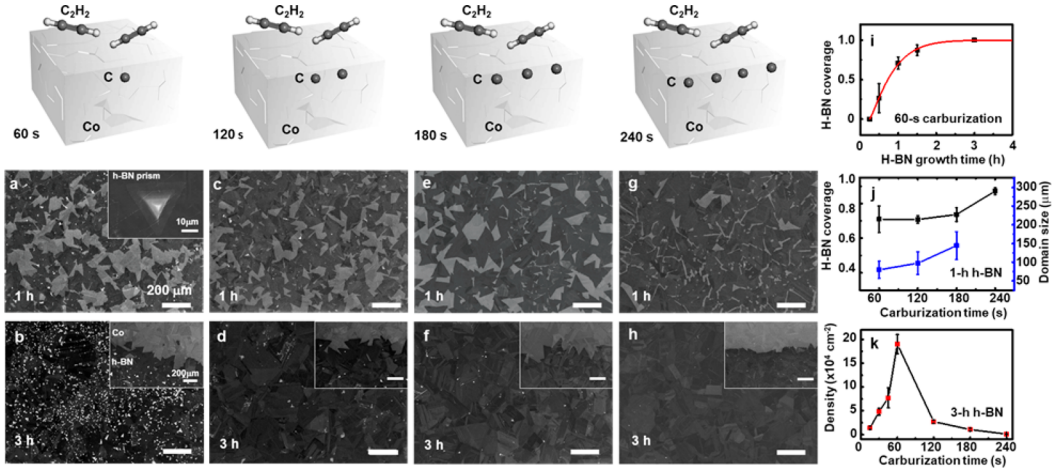

Figure 1. Morphology evolution of h-BN as a function of carburization time. Schematic shows that carbon concentration is controlled by carburization process duration. (**a**-**h**) Large-area SEM images of (**a**, **c**, **e**, **g**) 1-h h-BN samples (C1, 2, 3, 4) and (**b**, **d**, **f**, **h**) 3-h h-BN samples (D4, 5, 6, 7) on the Co substrate carburized for 60, 120, 180, and 240 s, respectively. Inset in (**a**) shows a typical "prism" shaped adlayer. Insets in (**b**, **d**, **f**, **h**) show the edge area for contrast. (**i**) Plot of h-BN fractional coverage as a function of h-BN growth time with carburization time fixed at 60 s, fitted with the JMAK model in red. (**j**) Plot of fractional coverage and domain size of 1-h h-BN samples as a function of carburization time from 60 to 240 s. (**k**) Density of prism-shaped island in the 3-h h-BN samples as a function of carburization time. The scale bar in (a) inset is 10 μm, and all others are 200 μm.

dissolution of carbon atoms in Co enabled and enhanced the direct growth of h-BN on the Co surface. A scanning electron microscopy (SEM) study of h-BN grown on Co with different carburization levels shows that the morphology as well as the lateral growth speed of the h-BN domains can be readily controlled by carbon concentration. The morphology varies from 2D layer-plus-3D islands to homogeneous 2D layers. Comprehensive characterizations including transmission electron microscopy (TEM), Raman spectroscopy, atomic force microscope (AFM), UV−vis absorption spectroscopy, and X-ray photoelectron spectroscopy (XPS) were carried out to study the structural and compositional properties of the samples. H-BN dielectric properties were characterized based on Co(foil)/h-BN/Co(contact) devices. Density functional theory (DFT) studies show enhanced adsorption and diffusion of both B and N atoms on the Co metal surface as a result of embedded carbon interstitials, which shed light on the role of carbon interstitials in transition metal substrates for reliable and controllable growth of large-area 2D h-BN.

As-received Co and Ni foils were polished, cleaned, and transferred to the MBE for growth (Methods), using a growth procedure illustrated in Figure S1 of the Supporting Information. The Co surfaces are dominated with (111) orientation, as can be seen from an X-ray diffraction pattern of as-grown samples (Figure S2 of the Supporting Information). Table S1 in the Supporting Information summarizes the growth conditions of all h-BN samples on pristine Co (Sample A), carburized Co substrates (Samples B1−B5, C1−C4, and D1−D7), and carburized Ni substrates (Samples E1−E2) that are described here. Direct growth of h-BN on pristine Co was reported previously, however, those h-BN films were grown at a relatively low temperature of 850 °C; thus the quality of the films was good but not excellent, which is inferred from a breakdown electric field of only 3 MV/cm.[31] In this work, all samples were grown at a higher substrate temperature of 900 °C in order to enhance the quality of the films. Surprisingly, with all other growth conditions the same as or similar to that used in ref 31, the attempt toward the growth of h-BN onto the pristine Co substrate at 900 °C led to no growth of any material on the surface (for example, Sample A), as verified by characterizations such as SEM, optical microscopy, Raman, and XPS (Figure S3 in the Supporting Information). The main reason is associated with high desorption of B on the metal surface, which is later confirmed by the theoretical calculation of adsorption energy. On the other hand, h-BN has been reliably grown onto all carburized Co substrates at 900 °C (Samples B1−B5, C1−C4, D1−D7). Vacuum carburization has been widely used for synthesis of carbon steel by exposing iron in a hydrocarbon environment.[36] Here, carburization of Co substrates was performed by introducing C_2H_2 gas with various flux rates and time at the growth temperature to attain different amounts of carbon incorporation in the substrates, as detailed in the Method section.

Figure 1a-h shows SEM images of h-BN samples grown for 1 h (Samples C1−C4) and 3 h (Samples D4-D7) on Co carburized from 60 to 240 s, respectively. The cartoons on top of SEM images indicate relative interstitial carbon concentration in the substrates of these samples, respectively. As seen from Figure 1a and b, high-density bright prism-shaped h-BN multilayer features are formed on these 60-s carburized samples grown for 1 and 3 h, respectively. The inset SEM image in Figure 1a shows a typical prism-shaped multilayer h-BN island, which appears as a bright feature in the SEM image due to the charging effect. The inset SEM image of the edge area of the sample in Figure 1b infers that the 3-h growth led to continuous h-BN 2D film, in contrast to partial 2D h-BN coverage in the 1-h h-BN sample, as shown in Figure 1a. The exposed Co area appears to be brighter due to less secondary electrons generated from h-BN/Co than from Co.[37] Additional evidence for the continuous nature of a 3-h h-BN film on the Co substrate is shown in Figure S9 of the Supporting Information. By fixing the Co carburization time at 60 s, additional samples (Samples B1−B5) with other h-BN growth times were grown, and Figure S4a-e shows SEM images of these samples. Only sparse h-BN nuclei emerge on the surface of a 15 min h-BN growth sample (Figure S4a), which suggests the time to form stable nuclei (incubation time) is around 15 min. Nucleation density increases rapidly in the next 15 min

DOI: 10.1021/acs.nanolett.7b05179
Nano Lett. 2018, 18, 3352−3361

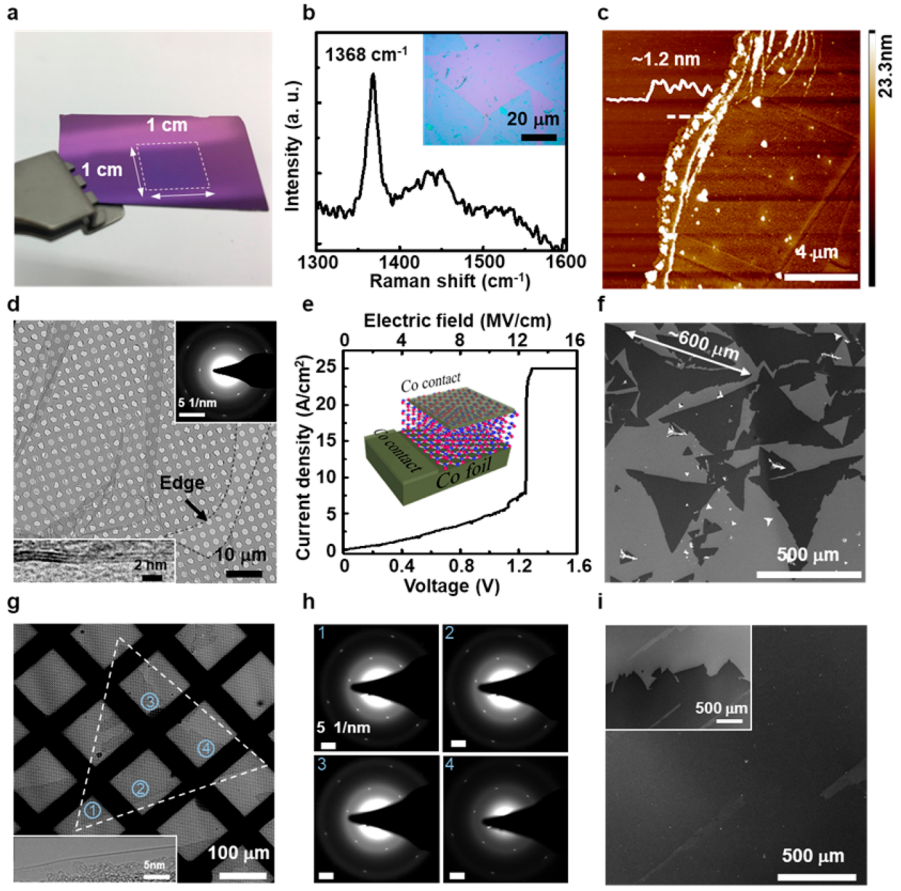

Figure 2. Characterization of large-area h-BN 2D layers. (**a-e**) show results of an h-BN sample grown on the carburized Co substrate (Sample D7), and (**f-h**) show results of h-BN samples grown on carburized Ni substrates. (**a**) Photograph of the h-BN sample transferred onto the SiO_2/Si substrate showing the uniform film with a size of 1 cm × 1 cm limited by the substrate holder. (**b**) Raman spectrum measured on the transferred h-BN few-layers on SiO_2/Si. The inset displays the optical microscope image of the corresponding sample. (**c**) AFM image scanning across the sample edge. (**d**) Plane view TEM image of the h-BN sample transferred onto a holey carbon film coated copper grid, with an SAED pattern shown in the top right corner inset and TEM image at the edge of the h-BN sample in the bottom left corner inset. (**e**) Plot of current density as a function of voltage and electric field of a Co(foil)/h-BN/Co(contact) two-terminal device with the inset displaying a schematic of the device structure. (**f**) SEM image of an h-BN sample grown on a 180-s carburized Ni substrate (Sample E1). Single-crystal h-BN flakes with a typical edge length up to ~600 μm are shown. (**g**) Plane view TEM image of one such flake of Sample E1 transferred onto a copper grid coated with holey carbon film with the inset displaying a TEM image at the edge of the flake. (**h**) SAED pattern at 4 different locations across the h-BN flake in **g** indicated by 1−4. (i) SEM image of an h-BN sample grown on a 300-s carburized Ni substrate (Sample E2) with the SEM image of the edge area of the sample in the inset, demonstrating large-area continuous uniform 2D h-BN film on carburized Ni.

growth following the incubation period (Figure S4b). After certain surface coverage, the size of most h-BN domains continues to increase as incoming adatoms are more likely to be captured by existing h-BN flake edges and the Ostwald ripening process also plays a dominating role (Figure S4c, d). The Co surface is almost fully covered after 90 min of growth. Besides the lateral growth, prism-shaped ad-layers along the vertical direction are also formed favorably on the surface irregularities or defective sites. The density of these prisms increases as the growth time increases. After 3-h growth, high-density 3D prism-shaped islands are formed on the continuous 2D layers (Figure 1b and Figure S4e). Detailed SEM, AFM, Raman, and absorption characterizations of the sample under a 60-s carburization and a 3-h h-BN growth show that the 2D h-BN film has a thickness of ~1 nm, and the size of some prisms is ~10 μm in edge length and ~20 nm in height (Figure S5).

The lateral growth is further studied under the framework of the Johnson-Mehl-Avrami−Kolmogorov (JMAK) model. Figure 1i plots the h-BN coverage versus its growth time. H-BN coverage on Co was obtained by using ImageJ software as detailed in Figure S8 of the Supporting Information and can be fitted by an exponential curve according to the JMAK model[38,39]

$$A_{BN} = 1 - \exp(k(t - t_0)^n) \quad (1)$$

where A_{BN} is the h-BN fractional coverage, and k is the rate constant, which depends on both the nucleation rate and the domain growth rate. The index n is the Avrami exponent, which is related to the dimensionality of the system and time-dependent nucleation and growth rate. It can be expressed as $n = qd + B$, where q equals 1 for linear growth (reaction controlled) or 1/2 for parabolic growth (diffusion controlled), d stands for the dimensionality of the growth, and B is 0 for site-saturated nucleation and 1 for continuous nucleation with constant rate. Figure S4f (Supporting Information) shows the same data in Figure 1f but is plotted using Avrami coordinates. A linear relationship is seen. The extracted Avrami exponent is $n = 1.20 \pm 0.05$, suggesting a 2D site-saturated nucleation.[39] It is worth noting that the JMAK model is based on the assumption of constant nucleation rate or a fixed number of

DOI: 10.1021/acs.nanolett.7b05179
Nano Lett. 2018, 18, 3352−3361

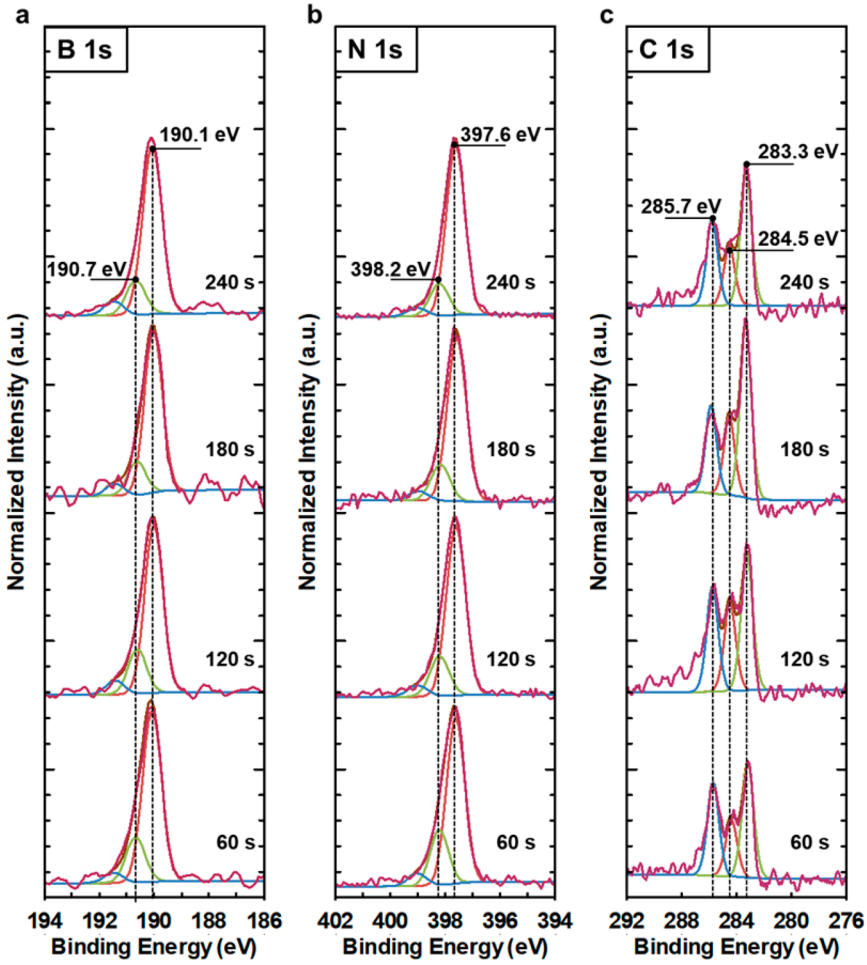

Figure 3. XPS of 1-h h-BN samples with different carburization times. (**a**-**c**) XPS spectra of surface resolved (**a**) B 1s, (**b**) N 1s, and (**c**) subsurface C 1s after removal of the h-BN layer and surface contamination by 60-s Ar ion sputtering of the h-BN samples with 60-, 120-, 180- and 240-s carburization time from bottom to top. **a** and **b** are plotted with a normalized range. **c** is normalized at the background of each spectrum.

nucleation sites, circular domain geometry, and constant, isotropic radial growth velocity.[40] Some modifications to the original JMAK model were done to apply to anisotropic radial growth.[41,42] Based on the fact that the present experimental data fit well with eq 1, it is reasonable to apply this model for the growth of h-BN, which does not grow isotropically.

With the change of carburization time from 60 to 240 s, the morphology of h-BN films grown for the same growth time of 1 h is evidently different as shown in Figure 1a, c, e, and g. H-BN flakes appear as dark features and increase in size and coverage as the carburization time increases. Figure 1j shows the average h-BN domain size and h-BN fractional coverage as a function of carburization time for these 1-h h-BN samples. The domain size increases from ∼80 to ∼144 μm as the carburization time increases from 60 to 180 s. For the sample with a 240-s carburization time (Figure 1g), h-BN domains coalesce and almost fully cover the Co surface. This implies that the lateral growth rate increases as the increase of the carburization time.

As the h-BN growth time is extended to 3 h, the entire Co surface of all samples with different carburization times (Samples D1−D7) is covered by continuous 2D h-BN films, as seen from the SEM images in Figure 1b, d, f, h and Figure S10. Additional 3D h-BN prism-shaped islands are also formed on top of the 2D layers in some of these samples, which are clearly dependent on the carburization time. Figure 1k shows the density of h-BN prisms as a function of carburization time. The density of h-BN prisms decreases from 1.9×10^5 cm^{-2} to roughly zero as the Co carburization time increases from 60 to 240 s. In contrast, the density of prisms increases gradually for shorter carburization time from 15 to 60 s. As discussed later, the incorporation of interstitial carbon in Co essentially enables the nucleation and growth of h-BN. As the interstitial carbon content is low in these samples with the carburization time less than 60 s, the adsorption of both B and N atoms is weak, and the nucleation mainly relies on defects and imperfection sites on the surface, which facilitates vertical growth of prisms. As the interstitial carbon content increases in the samples with carburization time larger than 60 s, the abundance of B and N atoms on the surface as a result of the enhanced adsorption facilitates the nucleation of h-BN domains. As shown later, the diffusion of these atoms is also enhanced as a result of the carbon interstitial effect. These factors are responsible for an increased lateral growth rate and domain size, thus prism-like island formation is further suppressed, leading to the dominant growth of 2D layers.

Figure 2a shows a photograph of a homogeneous few-layer h-BN sample (Sample D7). Figure 2b shows Raman spectrum of the transferred sample showing a sharp E_{2g} phonon mode at 1368 cm^{-1} and a fwhm of ∼16 cm^{-1}. The inset shows an optical microscopy image of the transferred film onto a SiO_2/Si substrate, indicating large-area uniform film. Figure 2c shows an AFM image of the transferred film with a scan profile across a

DOI: 10.1021/acs.nanolett.7b05179
Nano Lett. 2018, 18, 3352−3361

flake edge in the inset. The thickness of the h-BN film can be estimated as ~1.2 nm despite the undulating signals in the scan profile due to residual PMMA contamination from the transferring process. AFM images of several other samples after transferring can be found in Figure S11 of the Supporting Information, showing similar thickness. Figure 2d shows a plane view TEM image of the h-BN film transferred onto a holey carbon grid, and the top right inset is its corresponding 4-spot SAED pattern, indicating high crystallinity. Further TEM analysis of the film edge in the bottom left inset shows that the film consists of three layers.

Figure 2e shows current density versus voltage/electric field (J-V/E) of a Co(metal contact)/h-BN/Co(foil) two-terminal device with a metal contact size of 200 × 200 μm^2 based on a 240-s carburized h-BN sample (Sample D7). The thickness of the 2D h-BN is considered as ~1 nm according to the observation of a 3-layer film by TEM imaging (AFM result gives a slightly larger thickness of ~1.2 nm due to the tip effect). The J-V characteristic clearly exhibits a quasi-linear relationship at the low and moderate voltage regions due to direct tunneling[43] and a dielectric breakdown. The statistical study of J-V characteristics of 20 devices in Figure S13 in the Supporting Information leads to an average breakdown electric field of 9 MV/cm. This number is three times as large as that of our earlier devices based on h-BN films without carburization[31] and is comparable to those of exfoliated h-BN layers by a high-temperature high-pressure method,[44] suggesting significantly improved quality of the h-BN here.

The concept of carbon interstitial assisted growth of h-BN applies to other transition metal substrates. To avoid redundancy, we briefly show some results on carburized Ni substrates. Figure 2f shows the SEM image of a 6-h h-BN sample grown on a 180-s carburized Ni substrate (Sample E1). Discrete h-BN single-crystalline domains with an edge length of ~600 μm are evident, which are among the largest h-BN flakes ever reported.[16] The flakes grown near the edge of the substrate show an even larger size of ~700 μm in edge length (Figure S15 in the Supporting Information). The single-crystallinity is confirmed by recording SAED patterns at different locations across the h-BN domain, which are identical (Figure 2g,h). Additional information on TEM measurements showing the h-BN domain before and after transferring onto a TEM grid as well as additional SAED patterns at different spots can be found in Figures S14 and S15 in the Supporting Information. TEM imaging also reveals that the large h-BN domain is monolayer (Figure 2g). A large-area continuous uniform 2D h-BN film (Sample E2) was also achieved by the same 6-h h-BN growth on a Ni substrate with an increased carburization time of 300 s, as shown in the SEM image and inset of Figure 2h. To further confirm the continuous nature and thickness uniformity of the large-area h-BN film, large-area OM images together with large-area Raman mapping across a 1 cm × 1 cm area of the h-BN sample transferred on to a SiO_2/Si substrate are shown in Figure S16 of the Supporting Information.

Figure 3a and 3b show B 1s and N 1s XPS spectra of h-BN samples C1, C2, C3, and C4 which were grown for 1 h with carburization time from 60 to 240 s, respectively. The B 1s (N 1s) peak can be fitted into two peaks at a slightly different binding energy (BE), with a dominant peak at a lower BE of 190.1(397.6) eV as well as a small peak at a higher BE of 190.7(398.2) eV. The difference between the lower-BE and higher-BE peaks of the B 1s/N 1s peaks is ~0.6/0.6 eV, which is consistent with the reported values of 0.6 eV for B and 0.5 eV for N.[45] The dominant lower-BE peak can be assigned to the sp^2 B−N bond for hexagonal phase BN, and the higher-BE peak can be assigned to local cubic-like sp^3 bonds.[45−49] This assignment rather than other effects is discussed in detail in the Supporting Information. As seen from Figure 3a and 3b, the intensity of the 190.7(398.2) eV pair is the largest in the 60-s carburized sample. As the carburization time increases from 60 to 240 s, the intensity of the high-BE peak decreases. This result suggests the decrease of sp^3 bonds as the increase of the carburization time. Complementarily, the intensity of the lower BE pair (sp^2 bond phase) is inversely correlated to the prism density of each sample. This implies that the sp^3 bonds possibly exist in the prisms, seeding the vertical growth of multilayer prism-shaped islands, in particular in the low-carburized samples. The increase of interstitial carbon suppresses the formation of sp^3 type bonds and promotes the lateral growth of h-BN layers in higher-carburized samples. The stoichiometry of these as-grown films was calculated to have a B:N ratio between 1.05:1 and 1:1.06, which are essentially ~1:1 within the experimental error of the XPS sensitivity factors and peak fitting.

Figure 3c shows XPS C 1s spectra of samples C1, C2, C3, and C4 after 60-s Ar ion sputtering. This sputtering was used to completely remove h-BN layers and surface carbon contamination. Discussion on the depth-resolved XPS of the 240-s carburized sample is detailed as an example in Figure S17 of the Supporting Information. As seen from Figure 3c, a major peak at 283.3 eV is close to the assignment for interstitial carbon or carbide,[50−52] which indicates the presence of interstitial carbon atoms in the Co substrates. Compared with the XPS spectra of a reference pristine Co substrate and a pristine Co annealed at a temperature of 900 °C in H_2 environment for 1 h (Figure S18 in the Supporting Information), the increase of interstitial carbon atoms as a result of increased carburization is evident. However, it is noted that these results are collected at room temperature, under which Co has very low solubility of carbon, and the excessive carbon atoms over the solubility level would precipitate as α-C in between Co grains (Figure S6 in the Supporting Information). As a matter of fact, the solubility for carbon at the growth temperature is much higher, ~1.5 at % at 900 °C,[53] especially at the subsurface,[54−56] which will impact the growth mostly. Thus, with different C_2H_2 flux rate and treatment time, the interstitial carbon concentration can vary between 0 and 1.5 at % in different samples at the growth temperature, leading to different morphology of the synthesized films. The peak at 284.5 eV can be assigned to the C−C bond,[57] which possibly originated from the α-C structure embedded in Co grain boundaries (Figure S6 in the Supporting Information). B−C[58] and N−C[59] bonds are not detected in B 1s, N 1s, and C 1s spectra, which confirms the formation of h-BN without C incorporation or contamination.

To understand the effect of Co and carburized Co on the growth of h-BN at the molecular level, ab initio DFT simulations were performed. The simulation methodology is summarized in the Methods section. The surface energy of the substrate σ is defined as[60−62]

$$\sigma = \frac{[E_{slab} - \sum N_i \mu_i]}{2A} \quad (2)$$

where E_{slab} is the total energy of the substrate calculated from first-principles, μ_i is the chemical potential of species i in the slab structure, N_i is the number of particles of the i-th element

DOI: 10.1021/acs.nanolett.7b05179
Nano Lett. 2018, 18, 3352−3361

in the slab, and A is the area of the slab. The DFT calculations show that the Co(111) surface has a surface energy of 2037.87 mJ/m^2, compared to that of Cu(111), which is 1231.08 mJ/m^2. Cu(111) is used as a reference since h-BN can be grown on it.[2,10,11,12] The higher surface energy of Co(111) suggests better wettability of Co(111) as substrate.

The adsorption energy of B and N atoms on the Co substrate is calculated from the difference in total energies

$$E_{ads} = E_{B/N} + E_{surface} - E_{B/N\ on\ surface} \quad (3)$$

where $E_{B/N\ on\ surface}$ is the total energy of the adsorbed system, in which a boron or nitrogen atom is adsorbed on the Co(111) surface, $E_{B/N}$ is the chemical potential of the adsorbed B or N atom, and $E_{surface}$ is the energy of the Co(111) surface. A larger adsorption energy indicates stronger adsorption of an atom onto a surface, and a positive adsorption energy corresponds to stable adsorption. Figure 4 summarizes the DFT calculated

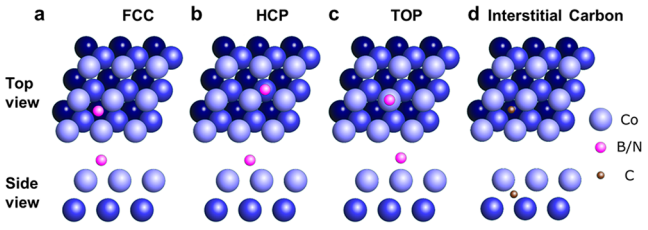

e

Adsorption Energy eV/atom	Boron			Nitrogen		
	FCC	HCP	Top	FCC	HCP	Top
Cu(111)	-1.74	-1.71	-3.26	-1.11	-1.19	-3.22
Co(111)	-0.80	-0.69	-2.23	0.26	0.50	-1.80
Co(111) With interstitial carbon	-0.522	-0.081	Not stable	0.298	1.062	Not stable

Figure 4. DFT calculation results of adsorption energies of B and N on Co(111) with and without embedded interstitial carbon. (**a**-**d**) Top view and side view schematic of (**a**) B/N atoms on FCC sites, (**b**) B/N atoms on HCP sites, (**c**) B/N atoms on top of substrate atoms, and (**d**) interstitial carbon on an octahedral site of the substrate. (**e**) A summary of adsorption energies of B and N on a reference Cu(111) substrate and on Co(111) substrates with and without an embedded interstitial carbon.

adsorption energies of B and N atoms on Co(111) with and without embedded interstitial carbon and on Cu(111) substrates. Top view and side view schematic of the atomic positions is shown in Figures 4a–4d. Positions to hold either B or N atoms include those directly above the hexagonally aligned Co (or Cu) atoms and the six voids within the Co (or Cu) hexagon, three of them designated as Face Centered Cubic (FCC) sites and the other three designated as Hexagonal Closely Packed (HCP) sites. On the Cu(111) surface, the adsorption energy of B and N is small and negative for all sites. Negative adsorption energies for B and N on the Cu(111) surface suggest that h- BN should not be formed on Cu(111) unless the growth is triggered through other mechanisms. The experimental demonstration of the growth of h-BN on Cu(111) was explained by the presence of preferential nucleation sites, for example, atomic steps and defects, including extended defects such as grain boundaries and point defects.[60−62] On the Co(111) surface, as seen from Figure 4e, the adsorption energies of B and N on the three sites are significantly higher compared to the Cu(111) surface. In addition, the adsorption energies of N on both the HCP and FCC sites of the Co surface are positive, suggesting enhanced adsorption of N atoms onto these sites of the substrate. The above comparison between Co and Cu substrates indicates that h-BN would be more likely to grow on Co under certain conditions such as at a relatively low growth temperature assuming both substrates are free of surface irregularities as preferential nucleation sites.

As the growth temperature is raised to a certain point such as 900 °C in this case, the desorption rates of both B and N atoms on the Co(111) surface become higher, leading to zero growth as shown earlier. The central theme of this work is to enable the growth of h-BN at these conditions by enhancing the adsorption and diffusion of B and N atoms on Co(111) using carbon interstitials in the substrate. In the XPS studies in Figure 3, we have shown the existence of interstitial carbon in Co. It was also reported that the octahedral sites in Co(111) are the most stable sites for interstitial carbon.[63] Thus, with the assumption of an interstitial carbon at the octahedral site in a supercell of Co(111), which is 0.6 Å below the surface, adsorption energies of different sites for B and N were calculated using the same DFT calculation method summarized in the Methods section. As seen from Figure 4e, except for the top site where both B and N are pushed away and hence can be considered unstable, the adsorption energies of B and N are further increased for HCP and FCC sites compared to no interstitial carbon. In particular, both B and N atoms prefer to adsorb at the HCP sites with the highest adsorption energy of −0.08 and 1.06 eV/atom, respectively.

From the above experiment and simulation results, we can rationalize the growth control from the perspective of adsorption energy. According to the framework of the Robinson and Robins model regarding nucleation,[39,64] when nucleation is limited by the desorption of surface adatoms, the saturation nucleation density N_s can be expressed as

$$N_s \propto N_{s0} \exp\left(-\frac{E_a}{2kT}\right) \quad (4)$$

where $E_a = E_{diff} - E_{ads} - E_{att}$ is the nucleation activation energy, and it is related to the adsorption energy E_{ads}, diffusion activation energy E_{diff}, and energy barrier of attachment for the capture of a surface adatom by a supercritical nucleus E_{att}. N_{s0} is a pre-exceptional term, which is related to the impinging rate of B/N atoms onto the surface and the density of nucleation sites. As seen from eq 4, at a given temperature and source flux, the increase of adsorption energy (E_{ads}) and attachment energy (E_{att}) and reduction of diffusion activation energy (E_{diff}) can promote the nucleation of h-BN. As seen from Figure 4, E_{ads} for B and N are 0.609 and 0.562 eV higher when interstitial carbon is present, which in turn have enhanced the nucleation of h-BN through eq 4.

To elaborate the carbon interstitial effect on diffusion activation energy (E_{diff}), simulation using the climbing image nudged elastic band (CI-NEB) method was carried out[65] (Methods). As seen from Figure S19 in the Supporting Information, E_{diff} is reduced by 0.079 and 0.207 eV for B and N atoms, respectively, after the interstitial carbon is present in the substrate, leading to the increase of nucleation of h-BN as well according to eq 4. The carbon interstitial effect on the attachment energy (E_{att}) remains elusive. Hypothetically, the change of E_{att} may not be as significant as the other energy terms since it is largely correlated to the formation energy of the B−N bond, which is assumed to be constant.

DOI: 10.1021/acs.nanolett.7b05179
Nano Lett. 2018, 18, 3352−3361

On pristine Co substrates, the low and negative adsorption energy of B atoms on the Co surface means a low B atomic sticking coefficient, leading to a low h-BN growth probability and reliability. Higher desorption of both B and N atoms on the Co surface at higher substrate temperatures further reduces the possibility of the growth. The existence of interstitial carbon atoms in Co assists the adsorption and diffusion of B and N atoms on the Co surface and thus enhances the nucleation of h-BN. As interstitial carbon concentration in Co is low, the h-BN nucleation relies mostly on imperfections such as defects, grain boundaries, and local valleys/protrusions on the surface. This condition results in the formation of both 2D h-BN and 3D prism-shaped islands, as discussed in the XPS analysis. The competition between 2D and 3D growth modes is clearly demonstrated from the effect of the carburization level on the density of prism-shaped islands (Figure 1k). On the other hand, as interstitial carbon concentration is high, h-BN nucleation happens uniformly across the surface as a result of abundant B and N atoms on the surface. In addition, an increased mobility of B and N atoms suppresses the vertical growth of 3D islands and promotes the 2D growth of uniform few-layer h-BN films through the preferential nucleation at the edges of growing flakes and Ostwald ripening processes. There is also negligible possibility that the h-BN would have been formed through precipitation growth mode under the current experimental condition (section 23 in the Supporting Information).

In conclusion, a new dimension of control in the growth of h-BN by modifying the transition metal substrates via carburization has been achieved. A systematic SEM study of MBE grown h-BN on carburized Co foils is presented to reveal the h-BN nucleation and domain growth and evolution of morphology as a function of carbon interstitial concentration in Co. The interstitial carbon atoms in Co trigger and enhance the growth of h-BN at the given condition. A further increase of the carbon concentration promotes lateral growth of h-BN few-layers and eliminates the prism-shape island formation. The lateral h-BN growth is fitted with the JMAK model. Characterizations were carried out on a few-layer h-BN sample grown on a 240-s C_2H_2 treated Co substrate, revealing that a trilayer h-BN film with good uniformity in thickness and a breakdown electric field of 9 MV/cm is formed. Single-crystalline h-BN flakes of ~600 μm and large-area uniform h-BN monolayer were achieved on carburized Ni substrates. The growth mechanism is further studied by DFT calculations. The adsorption and diffusion of both B and N atoms are enhanced by the existence of interstitial carbon atoms in the substrate, resulting in a reliable and controllable growth of 2D h-BN in contrast to no growth on pristine Co. The concept proposed and demonstrated here, namely interstitial-assisted growth of h-BN 2D films, not only paves the way for reliable synthesis of high-quality, large-area, uniform 2D h-BN for various applications but also can be applied to advance the synthesis of other 2D crystal materials.

Methods. *Substrate Preparation.* Co and Ni foils with a thickness of 0.1 mm and a purity of 99.995% from Alfa Aesar were polished on a SBT 920 Lapping and Polishing workstation and cut into 1 cm × 1 cm pieces as substrates. These pieces were degreased and deoxidized with acetone, IPA, and diluted hydrochloric acid (10%), rinsed in deionized (DI) water, blown dry, and finally loaded into an MBE chamber. A negligible amount of carbon impurities existed in as-received Co foils (0–6 ppm according to Alfa Aesar' glow discharge mass spectrometry report). Co substrates without the carburization process are referred to as pristine Co.

Hydrogen Annealing and Carburization. A redesigned PerkinElmer MBE system with a background pressure of ~10^{-9} Torr was used for the sample growth. The substrate was heated to 900 °C and annealed at this temperature under a 10-sccm flow of hydrogen gas for 10 min. Then, 0.5-sccm C_2H_2 gas was introduced into chamber with a pressure of 5×10^{-5} Torr for 15 to 240 s to enrich Co with carbon prior to h-BN growth. H-BN growth step started after the carburization process.

H-BN Growth. A Knudsen effusion cell filled with B_2O_3 powder (Alfa Aesar, 99.999% purity) was used as boron (B) source. Nitrogen plasma (Airgas, 99.9999% purity) generated by an electron cyclotron resonance (ECR) system and high-purity ammonia (American Gas Group, 99.9995% purity) were used as nitrogen (N) sources. The h-BN growth was conducted by simultaneous introduction of B and N sources onto the Co substrate at 900 °C. B cell temperature was maintained at 1150 °C. N sources consisting of 10-sccm N_2 gas through an ECR plasma source and NH_3 gas at a flow rate of 5 sccm through a shut-off valve were introduced to the chamber. The ECR current was set at 60 mA with a power of 228 W. The growth pressure was on the order of 6×10^{-4} Torr. After the growth, the samples were cooled to room temperature at a rate of 10 °C/min. Detailed growth conditions are summarized in Table S1 of the Supporting Information.

Transferring of h-BN Samples. The Co and Ni substrates were etched by $FeCl_3$/HCl solution after spin-coating PMMA (495 A4) on as-grown samples. The PMMA/h-BN stack was then transferred into 10% HCl, 5% HCl, and DI water successively to rinse out the residual etchant. The floating h-BN film was taken out by a desired substrate and left to dry for at least 12 h. After that, a few drops of PMMA were deposited again on the transferred film and soaked for another 2 h. The additional PMMA is used to soften the previous PMMA layer and enhance the attachment of h-BN on the substrate. PMMA was removed by dipping the sample into acetone bath. Finally, the sample was annealed at 400 °C inside a CVD furnace for 3 h in Ar/O_2 flow of 300 sccm to remove any remaining organic residue.

Characterizations. SEM images were acquired using an FEI NNS450 system in secondary electron (SE) imaging mode with a beam voltage of 10 kV. Raman characterizations were performed using a HORIBA LabRam system equipped with a 60 mW, 532 nm green laser. XPS characterization was conducted using a Kratos AXIS ULTRA XPS system equipped with an Al Kα monochromatic X-ray source and a 165 mm mean radius electron energy hemispherical analyzer. The fitting of XPS data was performed using CasaXPS software. As-measured XPS data was first calibrated by using Co $2p_{3/2}$ peak at 778.1 eV (Lorentzian Asymmetric line shape). B 1s, N 1s, and C 1s peaks were convoluted with Gaussian/Lorentzian line shape after being background-corrected by Shirley type background. AFM images were obtained using a Veeco D5000 AFM system. TEM images and selected area electron diffraction (SAED) patterns were acquired using a FEI Tecnai12 system. The TEM sample was prepared by picking a transferred h-BN film using a 200-mesh Cu grid covered with holey carbon film with an orthogonal array of 1.2-μm diameter holes.

Device Fabrication and Electrical Measurement. Co(foil)/h-BN/Co(contact) two-terminal devices were fabricated by a standard photolithography and lift-off process. A Co layer of

DOI: 10.1021/acs.nanolett.7b05179
Nano Lett. 2018, 18, 3352–3361

100 nm was patterned as top square contacts with an edge length of 200 μm on the surface of as-grown h-BN film. Reactive ion etching (RIE) was performed with a 50-sccm SF_6 plasma, under a power of 50 W, and for 15 s to etch the h-BN film between devices, which ensured isolation of different devices on the same substrate. Current−voltage (I−V) characteristics were obtained by an Agilent 4155C semiconductor parameter analyzer equipped with probing tips having a diameter of about 5 μm (Signatone, SE-TL).

DFT Calculations. First-principles density functional theory (DFT) calculations used the projector augmented wave method and the Perdew−Burke−Ernzerhof (PBE) type generalized gradient approximation[66,67] as implemented in the software package VASP.[68] Spin polarization was included self-consistently in all calculations. For the unit cell calculations, a Monkhorst−Pack scheme was adopted to integrate over the Brillouin zone with a k-mesh of 9 × 9 × 1. A plane-wave basis cutoff of 550 eV was used. All structures were optimized until the largest force on the atoms was less than 0.01 eV/Å. To model the adsorption energies of B and N atoms on the Co(111) surface, a single B or N atom was placed on specific sites of the surface of a supercell consisting of four atomic layers of 4 × 4 Co atoms in the (111) plane. These sites include the top of the Co atoms, hexagonal closely packed (HCP), and face centered cubic (FCC) sites of the Co(111) surface, on which the adsorption of B or N atoms would enable an epitaxial relationship between h-BN and the Co(111) substrate. A vacuum gap of 15 Å was introduced to avoid interactions between the periodically repeated surfaces. To simulate the diffusion activation energies, we adopted the climbing image nudged elastic band (CI-NEB) method[65]. The spring force between adjacent images was set to 5.0 eV/Å. The migration energies, namely diffusion activation energies, were obtained for the different adsorbates between the different sites of the Co(111) surface. The initial and final positions of the adsorbed atoms were set at two HCP sites of the surface. Eight images were considered to calculate the activation energies between the initial and final states.

■ ASSOCIATED CONTENT

Supporting Information

The Supporting Information is available free of charge on the ACS Publications website at DOI: 10.1021/acs.nanolett.7b05179.

MBE growth steps and conditions; discussion on nitrogen source and boron source; XRD pattern of as-grown h-BN sample; characterization of pristine reference sample; time-dependent growth of h-BN; characterization of a typical 2D layer-plus-3D islands sample; trace of carbon in Co substrate; additional Raman mapping of graphene G peak; measurement of h-BN coverage and prism-shaped island density; additional evidence of continuous nature of h-BN films; additional SEM images showing h-BN growth with shorter carburization time; AFM images of other h-BN transferred samples and an as-grown sample; statistics of h-BN breakdown electric field; additional electron diffraction patterns of an h-BN flake in the center and at the edge of the sample; an additional SEM image of h-BN on carburized Ni; Raman mapping of a sample of 1 cm × 1 cm area showing continuous nature and high thickness uniformity over large area; detail of the depth-resolved XPS, discussion of XPS B 1s and N 1s peaks and comparison of C 1s peaks from h-BN samples and reference substrates; result of diffusion activation energy calculation; discussion of possible growth of h-BN through precipitation (PDF)

■ AUTHOR INFORMATION

Corresponding Author

*Phone: 1-9518277131. Fax: 1-9518272425. E-mail: jianlin@ece.ucr.edu.

ORCID

Hao Tian: 0000-0001-5893-2319

Jianlin Liu: 0000-0001-6513-0867

Author Contributions

†H.T. and A.K. contributed equally to this work.

Author Contributions

J.L. led the project. H.T. and A.K. designed and performed the experimental works. P.D. and R.L. carried out DFT calculations. R.J.Z. performed TEM imaging. W.H.S. performed absorption measurements. Z.J.C. and Z.G.X. contributed to electrical measurements and analysis. Y.W.H. contributed to sample transferring. H.T. and J.L. wrote the manuscript. All authors contributed to analyzing and reviewing the data in this manuscript and commented on the manuscript.

Notes

The authors declare no competing financial interest.

■ ACKNOWLEDGMENTS

We acknowledge the support by FAME, one of six centers of STARnet, a Semiconductor Research Corporation program supported by MACRO and DARPA. This work was supported in part by SHINES, an Energy Frontier Research Center funded by the US Department of Energy, Office of Science, Basic Energy Sciences under Award #SC0012670. This work also used the Extreme Science and Engineering Discovery Environment (XSEDE), which is supported by National Science Foundation grant number ACI-1548562 through allocation number TG-DMR130081.

■ REFERENCES

(1) Nag, A.; Raidongia, K.; Hembram, K. P.; Datta, R.; Waghmare, U. V.; Rao, C. Graphene Analogues of BN: Novel Synthesis and Properties. *ACS Nano* **2010**, *4*, 1539−1544.

(2) Song, L.; Ci, L.; Lu, H.; Sorokin, P. B.; Jin, C.; Ni, J.; Kvashnin, A. G.; Kvashnin, D. G.; Lou, J.; Yakobson, B. I.; Ajayan, P. M. Large Scale Growth and Characterization of Atomic Hexagonal Boron Nitride Layers. *Nano Lett.* **2010**, *10*, 3209−3215.

(3) Watanabe, K.; Taniguchi, T.; Kanda, H. Direct-bandgap Properties and Evidence for Ultraviolet Lasing of Hexagonal Boron Nitride Single Crystal. *Nat. Mater.* **2004**, *3*, 404.

(4) Dean, C. R.; Young, A. F.; Meric, I.; Lee, C.; Wang, L.; Sorgenfrei, S.; Watanabe, K.; Taniguchi, T.; Kim, P.; Shepard, K. L.; Hone, J. Boron Nitride Substrates for High-Quality Graphene Electronics. *Nat. Nanotechnol.* **2010**, *5*, 722−726.

(5) Britnell, L.; Gorbachev, R.; Jalil, R.; Belle, B.; Schedin, F.; Mishchenko, A.; Georgiou, T.; Katsnelson, M.; Eaves, L.; Morozov, S.; Peres, N. M. R.; Leist, J.; Geim, A. K.; Novoselov, K. S.; Ponomarenko, A. Field-Effect Tunneling Transistor Based on Vertical Graphene Heterostructures. *Science* **2012**, *335*, 947−950.

(6) Lee, K. H.; Shin, H.-J.; Lee, J.; Lee, I.-y.; Kim, G.-H.; Choi, J.-Y.; Kim, S.-W. Large-Scale Synthesis of High-quality Hexagonal Boron Nitride Nanosheets for Large-area Graphene Electronics. *Nano Lett.* **2012**, *12*, 714−718.

DOI: 10.1021/acs.nanolett.7b05179
Nano Lett. 2018, 18, 3352−3361

(7) Levendorf, M. P.; Kim, C.-J.; Brown, L.; Huang, P. Y.; Havener, R. W.; Muller, D. A.; Park, J. Graphene and Boron Nitride Lateral Heterostructures for Atomically Thin Circuitry. *Nature* **2012**, *488*, 627.
(8) Cassabois, G.; Valvin, P.; Gil, B. Hexagonal Boron Nitride is an Indirect Bandgap Semiconductor. Nat. *Nat. Photonics* **2016**, *10*, 262−266.
(9) Kubota, Y.; Watanabe, K.; Tsuda, O.; Taniguchi, T. Deep Ultraviolet Light-Emitting Hexagonal Boron Nitride Synthesized at Atmospheric Pressure. *Science* **2007**, *317*, 932−934.
(10) Kim, K. K.; Hsu, A.; Jia, X.; Kim, S. M.; Shi, Y.; Hofmann, M.; Nezich, D.; Rodriguez-Nieva, J. F.; Dresselhaus, M.; Palacios, T.; Kong, J. Synthesis of Monolayer Hexagonal Boron Nitride on Cu Foil Using Chemical Vapor Deposition. *Nano Lett.* **2012**, *12*, 161−166.
(11) Tay, R. Y.; Park, H. J.; Ryu, G. H.; Tan, D.; Tsang, S. H.; Li, H.; Liu, W.; Teo, E. H. T.; Lee, Z.; Lifshitz, Y.; Ruoff, R. S. Synthesis of Aligned Symmetrical Multifaceted Monolayer Hexagonal Boron Nitride Single Crystals on Resolidified Copper. *Nanoscale* **2016**, *8*, 2434−2444.
(12) Kidambi, P. R.; Blume, R.; Kling, J.; Wagner, J. B.; Baehtz, C.; Weatherup, R. S.; Schloegl, R.; Bayer, B. C.; Hofmann, S. In Situ Observations During Chemical Vapor Deposition of Hexagonal Boron Nitride on Polycrystalline Copper. *Chem. Mater.* **2014**, *26*, 6380−6392.
(13) Driver, M. S.; Beatty, J. D.; Olanipekun, O.; Reid, K.; Rath, A.; Voyles, P. M.; Kelber, J. A. Atomic Layer Epitaxy of h-BN (0001) Multilayers on Co (0001) and Molecular Beam Epitaxy Growth of Graphene on h-BN (0001)/Co (0001). *Langmuir* **2016**, *32* (11), 2601−2607.
(14) Ismach, A.; Chou, H.; Ferrer, D. A.; Wu, Y.; McDonnell, S.; Floresca, H. C.; Covacevich, A.; Pope, C.; Piner, R.; Kim, M. J.; Wallence, R. M.; Colombo, L.; Ruoff, R. S. Toward the Controlled Synthesis of Hexagonal Boron Nitride Films. *ACS Nano* **2012**, *6*, 6378−6385.
(15) Shi, Y.; Hamsen, C.; Jia, X.; Kim, K. K.; Reina, A.; Hofmann, M.; Hsu, A. L.; Zhang, K.; Li, H.; Juang, Z.-Y.; Dresselhaus, M. S.; Li, L.-J.; Kong, J. Synthesis of Few-Layer Hexagonal Boron Nitride Thin Film by Chemical Vapor Deposition. *Nano Lett.* **2010**, *10*, 4134−4139.
(16) Meng, J.; Zhang, X.; Wang, Y.; Yin, Z.; Liu, H.; Xia, J.; Wang, H.; You, J.; Jin, P.; Wang, D.; Meng, X.-M. Aligned Growth of Millimeter-Size Hexagonal Boron Nitride Single-Crystal Domains on Epitaxial Nickel Thin Film. *Small* **2017**, *13*, 1604179.
(17) Caneva, S.; Weatherup, R. S.; Bayer, B. C.; Brennan, B.; Spencer, S. J.; Mingard, K.; Cabrero-Vilatela, A.; Baehtz, C.; Pollard, A. J.; Hofmann, S. Nucleation Control for Large, Single Crystalline Domains of Monolayer Hexagonal Boron Nitride via Si-Doped Fe Catalysts. *Nano Lett.* **2015**, *15*, 1867−1875.
(18) Kim, S. M.; Hsu, A.; Park, M. H.; Chae, S. H.; Yun, S. J.; Lee, J. S.; Cho, D.-H.; Fang, W.; Lee, C.; Palacios, T.; Dresselhaus, M.; Kim, K. K.; Lee, Y. H.; Kong, J. Synthesis of Large-Area Multilayer Hexagonal Boron Nitride for High Material Performance. *Nat. Commun.* **2015**, *6*, 8662.
(19) Caneva, S.; Weatherup, R. S.; Bayer, B. C.; Blume, R.; Cabrero-Vilatela, A.; Braeuninger-Weimer, P.; Martin, M.-B.; Wang, R.; Baehtz, C.; Schloegl, R.; Meyer, J. C.; Hofmann, S. Controlling Catalyst Bulk Reservoir Effects for Monolayer Hexagonal Boron Nitride CVD. *Nano Lett.* **2016**, *16* (2), 1250−1261.
(20) Sutter, P.; Lahiri, J.; Zahl, P.; Wang, B.; Sutter, E. Scalable Synthesis of Uniform Few-Layer Hexagonal Boron Nitride Dielectric Films. *Nano Lett.* **2013**, *13*, 276−281.
(21) Kim, G.; Jang, A.-R.; Jeong, H. Y.; Lee, Z.; Kang, D. J.; Shin, H. S. Growth of High-Crystalline, Single-Layer Hexagonal Boron Nitride on Recyclable Platinum Foil. *Nano Lett.* **2013**, *13*, 1834−1839.
(22) Hao, Y.; Bharathi, M.; Wang, L.; Liu, Y.; Chen, H.; Nie, S.; Wang, X.; Chou, H.; Tan, C.; Fallahazad, B.; Ramanarayan, H.; Magnuson, C. W.; Tutuc, E.; Yakobson, B. I.; McCarty, K. F; Zhang, Y.-W.; Kim, P.; Hone, J.; Colombo, L.; Ruoff, R. S. The Role of Surface Oxygen in the Growth of Large Single-Crystal Graphene on Copper. *Science* **2013**, *342*, 720−723.
(23) Song, X.; Gao, T.; Nie, Y.; Zhuang, J.; Sun, J.; Ma, D.; Shi, J.; Lin, Y.; Ding, F.; Zhang, Y.; Liu, Z. Seed-Assisted Growth of Single-Crystalline Patterned Graphene Domains on Hexagonal Boron Nitride by Chemical Vapor Deposition. *Nano Lett.* **2016**, *16*, 6109−6116.
(24) Ismach, A.; Mende, P.; Dolocan, A.; Addou, R.; Aloni, S.; Wallace, R.; Feenstra, R.; Ruoff, R.; Colombo, L. Carbon-Assisted Chemical Vapor Deposition of Hexagonal Boron Nitride. *2D Mater.* **2017**, *4*, 025117.
(25) Zheng, R.; Xu, Z.; Khanaki, A.; Tian, H.; Zuo, Z.; Zheng, J.-G.; Liu, J. Low-Temperature Growth of Graphene on Iron Substrate by Molecular Beam Epitaxy. *Thin Solid Films* **2017**, *627*, 39−43.
(26) Cho, Y.-J.; Summerfield, A.; Davies, A.; Cheng, T. S.; Smith, E. F.; Mellor, C. J.; Khlobystov, A. N.; Foxon, C. T.; Eaves, L.; Beton, P. H.; Novikov, S. V. Hexagonal Boron Nitride Tunnel Barriers Grown on Graphite by High Temperature Molecular Beam Epitaxy. *Sci. Rep.* **2016**, *6*, 34474.
(27) Summerfield, A.; Davies, A.; Cheng, T. S.; Korolkov, V. V.; Cho, Y.; Mellor, C. J.; Foxon, C. T.; Khlobystov, A. N.; Watanabe, K.; Taniguchi, T.; Eaves, L.; Novikov, S. V.; Beton, P. Strain-Engineered Graphene Grown on Hexagonal Boron Nitride by Molecular Beam Epitaxy. *Sci. Rep.* **2016**, *6*, 22440.
(28) Nakhaie, S.; Wofford, J.; Schumann, T.; Jahn, U.; Ramsteiner, M.; Hanke, M.; Lopes, J.; Riechert, H. Synthesis of Atomically Thin Hexagonal Boron Nitride Films on Nickel Foils by Molecular Beam Epitaxy. *Appl. Phys. Lett.* **2015**, *106* (21), 213108.
(29) Wofford, J. M.; Nakhaie, S.; Krause, T.; Liu, X.; Ramsteiner, M.; Hanke, M.; Riechert, H.; Lopes, J. M. J. A hybrid MBE-Based Growth Method for Large-Area Synthesis of Stacked Hexagonal Boron Nitride/Graphene Heterostructures. *Sci. Rep.* **2017**, *7*, 43644.
(30) Xu, Z.; Khanaki, A.; Tian, H.; Zheng, R.; Suja, M.; Zheng, J.-G.; Liu, J. Direct Growth of Hexagonal Boron Nitride/Graphene Heterostructures on Cobalt Foil Substrates by Plasma-Assisted Molecular Beam Epitaxy. *Appl. Phys. Lett.* **2016**, *109*, 043110.
(31) Xu, Z.; Tian, H.; Khanaki, A.; Zheng, R.; Suja, M.; Liu, J. Large-Area Growth of Multi-Layer Hexagonal Boron Nitride on Polished Cobalt Foils by Plasma-Assisted Molecular Beam Epitaxy. *Sci. Rep.* **2017**, *7*, 43100.
(32) Xu, Z.; Zheng, R.; Khanaki, A.; Zuo, Z.; Liu, J. Direct Growth of Graphene on In Situ Epitaxial Hexagonal Boron Nitride Flakes by Plasma-Assisted Molecular Beam Epitaxy. *Appl. Phys. Lett.* **2015**, *107*, 213103.
(33) Zuo, Z.; Xu, Z.; Zheng, R.; Khanaki, A.; Zheng, J.-G.; Liu, J. In-Situ Epitaxial Growth of Graphene/h-BN van der Waals Heterostructures by Molecular Beam Epitaxy. *Sci. Rep.* **2015**, *5*, 14760.
(34) Zheng, R.; Khanaki, A.; Tian, H.; He, Y.; Cui, Y.; Xu, Z.; Liu, J. Precipitation Growth of Graphene under Exfoliated Hexagonal Boron Nitride to Form Heterostructures on Cobalt Substrate by Molecular Beam Epitaxy. *Appl. Phys. Lett.* **2017**, *111*, 011903.
(35) Khanaki, A.; Tian, H.; Xu, Z.; Zheng, R.; He, Y.; Cui, Z.; Yang, J.; Liu, J. Effect of High Carbon Incorporation in Co Substrates on the Epitaxy of Hexagonal Boron Nitride/Graphene Heterostructures. *Nanotechnology* **2018**, *29* (3), 035602.
(36) Kula, P.; Pietrasik, R.; Dybowski, K. Vacuum Carburizing—Process Optimization. *J. Mater. Process. Technol.* **2005**, *164-165*, 876−881.
(37) Xie, J.; Spallas, J. P. Different Contrast Mechanisms in SEM Imaging of Graphene; Technical Report; Agilent Technologies: 2012.http://www.toyo.co.jp/files/user/img/product/microscopy/pdf/5991-0782EN.pdf (accessed May 7, 2018) .
(38) Johnson, W. A.; Mehl, R. F. Reaction Kinetics in Process of Nucleation and Growth. *Transaction of AIME* **1939**, *135*, 416−458.
(39) Kim, H.; Mattevi, C.; Calvo, M. R.; Oberg, J. C.; Artiglia, L.; Agnoli, S.; Hirjibehedin, C. F.; Chhowalla, M.; Saiz, E. Activation Energy Paths for Graphene Nucleation and Growth on Cu. *ACS Nano* **2012**, *6*, 3614−3623.
(40) Weatherup, R. S.; Shahani, A. J.; Wang, Z.-J.; Mingard, K.; Pollard, A. J.; Willinger, M.-G.; Schloegl, R.; Voorhees, P. W.; Hofmann, S. In Situ Graphene Growth Dynamics on Polycrystalline Catalyst Foils. *Nano Lett.* **2016**, *16* (10), 6196−6206.

DOI: 10.1021/acs.nanolett.7b05179
Nano Lett. 2018, 18, 3352−3361

(41) Li, J.; Wang, J.; Xu, Q.; Yang, G. Comparison of Johnson−Mehl−Avrami−Kologoromov (JMAK) Kinetics with a Phase Field Simulation for Polycrystalline Solidification. *Acta Mater.* **2007**, *55* (3), 825−832.
(42) Kooi, B. J. Monte Carlo Simulations of Phase Transformations Caused by Nucleation and Subsequent Anisotropic Growth: Extension of the Johnson-Mehl-Avrami-Kolmogorov Theory. *Phys. Rev. B: Condens. Matter Mater. Phys.* **2004**, *70* (22), 224108.
(43) Lee, G.-H.; Yu, Y.-J.; Lee, C.; Dean, C.; Shepard, K. L.; Kim, P.; Hone, J. Electron Tunneling through Atomically Flat and Ultrathin Hexagonal Boron Nitride. *Appl. Phys. Lett.* **2011**, *99*, 243114.
(44) Hattori, Y.; Taniguchi, T.; Watanabe, K.; Nagashio, K. Layer-By-Layer Dielectric Breakdown of Hexagonal Boron Nitride. *ACS Nano* **2015**, *9*, 916−921.
(45) Schwarz, M.; Riss, A.; Garnica, M.; Ducke, J.; Deimel, P. S.; Duncan, D. A.; Thakur, P. K.; Lee, T.-L.; Seitsonen, A. P.; Barth, J. V.; Allegretti, F.; Auwärter, W. Corrugation in the Weakly Interacting Hexagonal-BN/Cu (111) System: Structure Determination by Combining Noncontact Atomic Force Microscopy and X-Ray Standing Waves. *ACS Nano* **2017**, *11* (9), 9151−9161.
(46) Koepke, J. C.; Wood, J. D.; Chen, Y.; Schmucker, S. W.; Liu, X.; Chang, N. N.; Nienhaus, L.; Do, J. W.; Carrion, E. A.; Hewaparakrama, J.; Rangarajan, A.; Datye, I.; Mehta, R.; Haasch, R. T.; Gruebele, M.; Girolami, G. S.; Pop, E.; Lyding, J. W. Role of Pressure in the Growth of Hexagonal Boron Nitride Thin Films from Ammonia-Borane. *Chem. Mater.* **2016**, *28* (12), 4169−4179.
(47) Panayiotatos, Y.; Logothetidis, S.; Handrea, M.; Kautek, W. Homogeneous and Amorphous Sputtered Sp3-Bonded BN Films at RT: a Stress, Spectroscopic Ellipsometry and XPS Study. *Diamond Relat. Mater.* **2003**, *12* (3−7), 1151−1156.
(48) Widmayer, P.; Boyen, H.-G.; Ziemann, P.; Reinke, P.; Oelhafen, P. Electron Spectroscopy on Boron Nitride Thin Films: Comparison of Near-Surface to Bulk Electronic Properties. *Phys. Rev. B: Condens. Matter Mater. Phys.* **1999**, *59*, 5233.
(49) Khanaki, A.; Xu, Z.; Tian, H.; Zheng, R.; Zuo, Z.; Zheng, J.-G.; Liu, J. Self-Assembled Cubic Boron Nitride Nanodots. *Sci. Rep.* **2017**, *7*, 4087.
(50) Bonzel, H. P.; Krebs, H. J. On the Chemical Nature of the Carbonaceous Deposits on Iron After CO Hydrogenation. *Surf. Sci.* **1980**, *91*, 499−513.
(51) Panzner, G.; Diekmann, W. The Bonding State of Carbon Segregated to α-iron Surfaces and on Iron Carbide Surfaces Studied by Electron Spectroscopy. *Surf. Sci.* **1985**, *160*, 253−270.
(52) Zhang, C.; Zhao, S.; Jin, C.; Koh, A. L.; Zhou, Y.; Xu, W.; Li, Q.; Xiong, Q.; Peng, H.; Liu, Z. Direct Growth of Large-area Graphene and Boron Nitride Heterostructures by a Co-Segregation Method. *Nat. Commun.* **2015**, *6*, 6519.
(53) Ishida, K.; Nishizawa, T. The C-Co (Carbon-Cobalt) System. *J. Phase Equilib.* **1991**, *12*, 417−424.
(54) van Helden, P.; Ciobîcă, I. M. A DFT Study of Carbon in the Subsurface Layer of Cobalt Surfaces. *ChemPhysChem* **2011**, *12* (16), 2925−2928.
(55) Jansen, A. P.; Agrawal, R.; Spanu, L. Thermodynamics and Kinetics of Carbon Deposits on Cobalt: a Combined Density Functional Theory and Kinetic Monte Carlo Study. *Phys. Chem. Chem. Phys.* **2016**, *18* (41), 28515−28523.
(56) Xu, J.; Saeys, M. First Principles Study of the Stability and the Formation Kinetics of Subsurface and Bulk Carbon on a Ni Catalyst. *J. Phys. Chem. C* **2008**, *112* (26), 9679−9685.
(57) Zheng, M.; Takei, K.; Hsia, B.; Fang, H.; Zhang, X.; Ferralis, N.; Ko, H.; Chueh, Y.-L.; Zhang, Y.; Maboudian, R.; Javey, A. Metal-catalyzed Crystallization of Amorphous Carbon to Graphene. *Appl. Phys. Lett.* **2010**, *96*, 063110.
(58) Shirasaki, T.; Derré, A.; Ménétrier, M.; Tressaud, A.; Flandrois, S. Synthesis and Characterization of Boron-Substituted Carbons. *Carbon* **2000**, *38* (10), 1461−1467.
(59) Wada, Y.; Yap, Y.; Yoshimura, M.; Mori, Y.; Sasaki, T. The Control of BN and BC Bonds in BCN Films Synthesized Using Pulsed Laser Deposition. *Diamond Relat. Mater.* **2000**, *9* (3−6), 620−624.
(60) Jensen, F.; Besenbacher, F.; Lægsgaard, E.; Stensgaard, I. Surface Reconstruction of Cu (110) Induced by Oxygen Chemisorption. *Phys. Rev. B: Condens. Matter Mater. Phys.* **1990**, *41*, 10233.
(61) Li, X.; Cai, W.; An, J.; Kim, S.; Nah, J.; Yang, D.; Piner, R.; Velamakanni, A.; Jung, I.; Tutuc, E.; Banerjee, S. K.; Colombo, L.; Ruoff, R. S. Large-Area Synthesis of High-Quality and Uniform Graphene Films on Copper Foils. *Science* **2009**, *324*, 1312−1314.
(62) Hasegawa, Y.; Avouris, P. Direct Observation of Standing Wave Formation at Surface Steps Using Scanning Tunneling Spectroscopy. *Phys. Rev. Lett.* **1993**, *71*, 1071.
(63) Liu, S.; van Duin, A. C.; van Duin, D. M.; Liu, B.; Edgar, J. H. Atomistic Insights into Nucleation and Formation of Hexagonal Boron Nitride on Nickel from First-Principles-Based Reactive Molecular Dynamics Simulations. *ACS Nano* **2017**, *11*, 3585−3596.
(64) Robinson, V.; Robins, J. Nucleation Kinetics of Gold Deposited onto UHV Cleaved Surfaces of NaCl and KBr. *Thin Solid Films* **1974**, *20* (1), 155−175.
(65) Henkelman, G.; Uberuaga, B. P.; Jónsson, H. A Climbing Image Nudged Elastic Band Method for Finding Saddle Points and Minimum Energy Paths. *J. Chem. Phys.* **2000**, *113* (22), 9901−9904.
(66) Perdew, J. P.; Burke, K.; Ernzerhof, M. Generalized Gradient Approximation Made Simple. *Phys. Rev. Lett.* **1996**, *77* (18), 3865.
(67) Ernzerhof, M.; Scuseria, G. E. Assessment of the Perdew−Burke−Ernzerhof Exchange-Correlation Functional. *J. Chem. Phys.* **1999**, *110* (11), 5029−5036.
(68) Kresse, G.; Hafner, J. Ab Initio Molecular Dynamics for Liquid Metals. *Phys. Rev. B: Condens. Matter Mater. Phys.* **1993**, *47* (1), 558.

DOI: 10.1021/acs.nanolett.7b05179
Nano Lett. 2018, 18, 3352−3361